



HAL
open science

Comparison of X-ray and optical measurements in the near-field of an optically dense coaxial air-assisted atomizer

Julie K Bothell, Nathanaël Machicoane, Danyu Li, Timothy R. Morgan, Alberto Aliseda, Alan L Kastengren, Theodore J Heindel

► **To cite this version:**

Julie K Bothell, Nathanaël Machicoane, Danyu Li, Timothy R. Morgan, Alberto Aliseda, et al.. Comparison of X-ray and optical measurements in the near-field of an optically dense coaxial air-assisted atomizer. *International Journal of Multiphase Flow*, 2020, 125, 10.1016/j.ijmultiphaseflow.2020.103219 . hal-02519242

HAL Id: hal-02519242

<https://hal.science/hal-02519242>

Submitted on 26 Mar 2020

HAL is a multi-disciplinary open access archive for the deposit and dissemination of scientific research documents, whether they are published or not. The documents may come from teaching and research institutions in France or abroad, or from public or private research centers.

L'archive ouverte pluridisciplinaire **HAL**, est destinée au dépôt et à la diffusion de documents scientifiques de niveau recherche, publiés ou non, émanant des établissements d'enseignement et de recherche français ou étrangers, des laboratoires publics ou privés.

1 **Comparison of X-ray and optical measurements in the near-field of an optically**
2 **dense coaxial air-assisted atomizer**

3 Julie K. Bothell^{a,*}, Nathanael Machicoane^b, Danyu Li^a, Timothy B. Morgan^a,
4 Alberto Aliseda^b, Alan L. Kastengren^c, Theodore J. Heindel^a

5 ^a*Center for Multiphase Flow Research and Education, Department of*
6 *Mechanical Engineering, Iowa State University, Ames, IA, USA*

7 ^b*Department of Mechanical Engineering, University of Washington, Seattle, WA, USA*

8 ^c*X-Ray Science Division, Advanced Photon Source, Argonne National Laboratory,*
9 *Lemont, IL, USA*

10 * *Corresponding author, jbothell@iastate.edu*
11

12 ABSTRACT

13 Understanding the near-field region of a spray is integral to optimization and control
14 efforts because this region is where liquid break-up and spray formation occurs, setting the
15 conditions under which the spray dynamics evolve under the gas turbulence and droplet inertia.
16 However, the high optical density of this region complicates measurements; thus, it is not yet
17 well characterized. This paper is intended to compare four of the leading experimental
18 techniques that are being used or developed to study the near-field region of a spray. These
19 techniques are shadowgraphy, tube source X-ray radiography, high-speed synchrotron white-
20 beam X-ray imaging, and synchrotron focused-beam X-ray radiography. Each of these methods
21 is applied to a canonical spray, using the same nozzle, under identical flow conditions.
22 Synchrotron focused-beam radiography shows that a time-averaged Gaussian liquid distribution
23 is a valid approximation very near the nozzle, before the core has broken apart. The Gaussian
24 behavior continues as the spray progresses further downstream, showing self-similarity. A spray
25 angle can be defined from the linear spreading of the Gaussian intensity distribution with
26 downstream distance. The spray angle found from shadowgraphy is validated with focused-beam

27 testing. Additionally, a novel method of estimating the intact length of the spray from different
28 X-ray techniques, that uses broadband illumination, is presented.

29 **Keywords:** Near-field spray characterization, Shadowgraph, Spray diagnostics, Synchrotron X-
30 ray radiography, X-ray flow visualization

31

32 **1. Introduction**

33 Coaxial atomizers are of interest in research because of their use as fuel injectors for gas
34 turbines and engines, two-phase chemical reactors, and food processing (Lasheras
35 and Hopfinger, 2000). Spray droplet characterization has been a primary focus of this research,
36 especially in the combustion community (Aggarwal, 1998; Law, 1982). Some of the methods
37 commonly used to study the far-field region of sprays include Laser Doppler Velocimetry
38 (LDV), Phase Doppler Particle Analysis (PDPA), and Particle Image Velocimetry (PIV).
39 However, each of these methods relies on the spray being broken into droplets, and are thus not
40 applicable for studying the near-field region. The near-field region is where instabilities begin to
41 develop, and is of utmost importance because of its role in setting up the primary combustion
42 zone (Lightfoot et al., 2015). Fully characterizing this region is difficult because the thick liquid
43 core reflects most visible light, impeding the use of most noninvasive measurement methods.
44 Thus, the near-field region has not been studied with the depth and rigor that has been applied to
45 the mid- or far-field region.

46 Shadowgraphy and back-illuminated imaging are often used for studying sprays
47 (Castrejón-García et al., 2011; Stevenin et al., 2012; Westlye et al., 2017). These visible light
48 techniques are useful in making qualitative assessments about the spray and obtaining a measure
49 of the core length, but it is challenging to estimate accurately other quantitative measurements,

50 such as spray angle. X-ray diagnostics have emerged recently as an alternative to optical
51 diagnostics for studying the near-field region (Heindel, 2018; Linne, 2013). Unlike visible light,
52 X-rays are able to penetrate the dense liquid region, and their attenuation is related to the path
53 length and density of the materials through which they pass. The attenuation can then be used to
54 measure (or estimate if the attenuation is from a broadband source) the quantity of liquid present
55 in the line of sight along the X-ray beam. An additional advantage of X-rays is the mild
56 refraction and diffraction at liquid-gas interfaces, which enhances visualization (Kastengren et
57 al., 2012). Ballistic imaging is another measurement technique that has been used to investigate
58 the spray near-field (Linne et al., 2009), but is not covered in this study.

59 To understand how the data from these measurement techniques compare, this study uses
60 an identical experimental setup and flow conditions to provide a side-by-side comparison of
61 multiple techniques. The four techniques used in this study are shadowgraphy (as the visible
62 light technique), tube source X-ray radiography, synchrotron white-beam phase-contrast
63 imaging, and synchrotron focused-beam radiography. Core length and spray angle are the two
64 major defining parameters of the spray near-field that are compared. An accurate measure for the
65 core length was found from shadowgraphy and a method that uses X-ray techniques to estimate
66 this length was developed. The spray angle was found from focused-beam radiography, and the
67 spray angles from the other three methods were compared to this measurement. Additionally, the
68 capabilities, advantages, and disadvantages of each technique are discussed. A complementary
69 study using an impinging jet spray and structured light and 3-D X-ray CT reconstruction was
70 completed by Halls et al. (2013). Using the same impinging jet spray setup, Halls et al. (2014)
71 compared 2-D and 3-D mass distribution measures to focused-beam measurements.

72

73 **2. Experimental setup**

74 *2.1 Nozzle and Flow Conditions*

75 The nozzle used in these experiments, shown in Fig. 1, is a canonical two-fluid coaxial
 76 atomizer (Machicoane et al, 2019). The liquid Reynolds number is defined by:

77
$$Re_l = (U_l d_l) / \nu_l \quad (1)$$

78 where $d_l = 2.1$ mm is the inner diameter of the liquid nozzle, ν_l is the kinematic viscosity of the
 79 liquid, and U_l is the liquid mean exit velocity, calculated as $U_l = Q_l / A_l$ where Q_l is the liquid flow
 80 rate and A_l is the exit area of the liquid nozzle. With $d_l = 2.1$ mm and a liquid nozzle length of
 81 110 mm, the length to diameter ratio is 52 ensuring a fully developed flow. The inner diameter of
 82 the gas nozzle at the exit is $d_g = 10$ mm, and the gas Reynolds number is defined by:

83
$$Re_g = 4Q_{tot} / (\pi d_{eff} \nu_g) \quad (2)$$

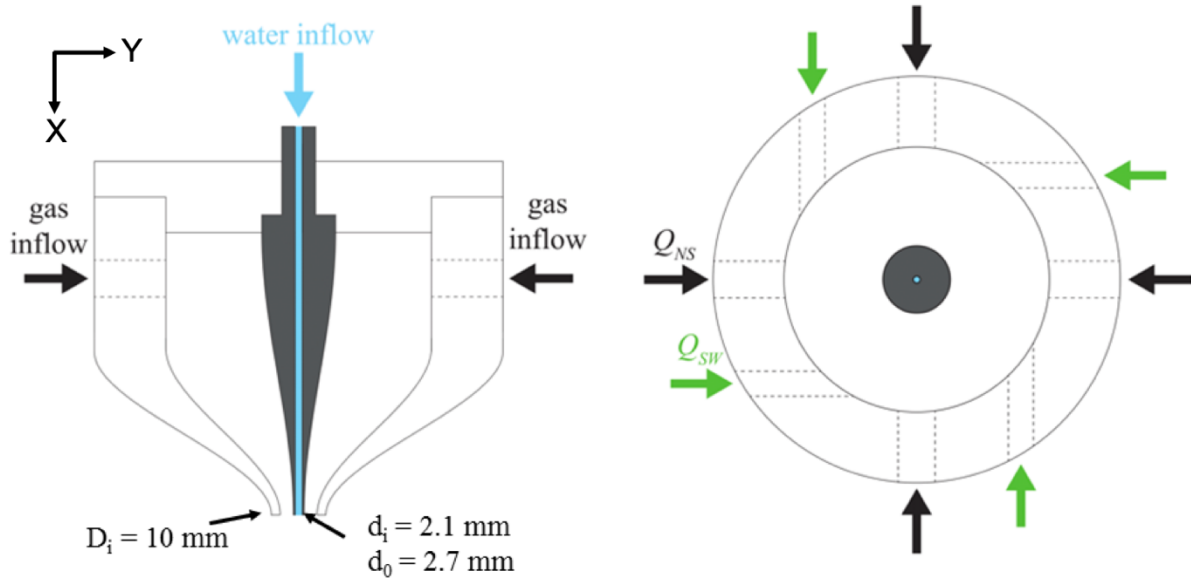
84 where Q_{tot} is the total gas flow rate, and ν_g is the kinematic viscosity of air. The effective inner
 85 diameter of the gas nozzle (d_{eff}) is defined as:

86
$$d_{eff} = (d_g^2 - D_l^2)^{1/2} \quad (3)$$

87 which is the diameter of a circle with the same exit area as the gas nozzle, and $D_l = 2.7$ mm is the
 88 outer diameter of the liquid nozzle. The total gas flow rate is composed of straight and swirl air.

89 As shown in Figure 1, straight air enters the gas plenum directed at the liquid needle centerline
 90 whereas swirl air enters the gas plenum tangent to the plenum wall (which is not used in the
 91 current study).

92



93

94 Figure 1: Nozzle schematic showing liquid and gas inlets of a two-fluid coaxial nozzle. Q_{NS}
 95 shows the locations for straight air flow and Q_{SW} shows how swirl air is added (this
 96 functionality is not utilized in the current study).

97

98 The momentum flux ratio (M) is defined by:

$$99 \quad M = (\rho_g U_g^2) / (\rho_l U_l^2) \quad (4)$$

100 where the subscripts g and l define the gas and liquid properties, respectively, and ρ is the fluid
 101 density. Additionally, the Weber number (We) and mass loading ratio (m) are defined by:

$$102 \quad We = \rho_g U_g^2 d_l / \sigma \quad (5)$$

$$103 \quad m = (\rho_l U_l A_l) / (\rho_g U_g A_g) \quad (6)$$

104 where σ is the interfacial tension.

105 All length scales have been nondimensionalized with d_l where appropriate; hence
 106 $Y = y/d_l$ is the spanwise coordinate and $X = x/d_l$ is the axial coordinate originating at the nozzle
 107 exit. The liquid flow rate is constant for all test conditions considered in this study, yielding a
 108 fixed Reynolds number of $Re_l = 1,100$ to ensure laminar flow, with a large We and small m to

109 ensure that the breakup and interfacial instabilities are driven by the gas (Lasheras et al., 1998;
 110 Lasheras and Hopfinger, 2000). The gas flow conditions selected for this study are summarized
 111 in Table 1.

112

113 Table 1: Gas Reynolds number, momentum flux ratio, Weber number, and mass loading for
 114 each condition used in this study.

Re_g	M	We	m
21,200	6.0	40.3	0.55
31,100	12.9	86.8	0.37
46,500	28.9	194.1	0.25
69,300	64.1	430.5	0.17

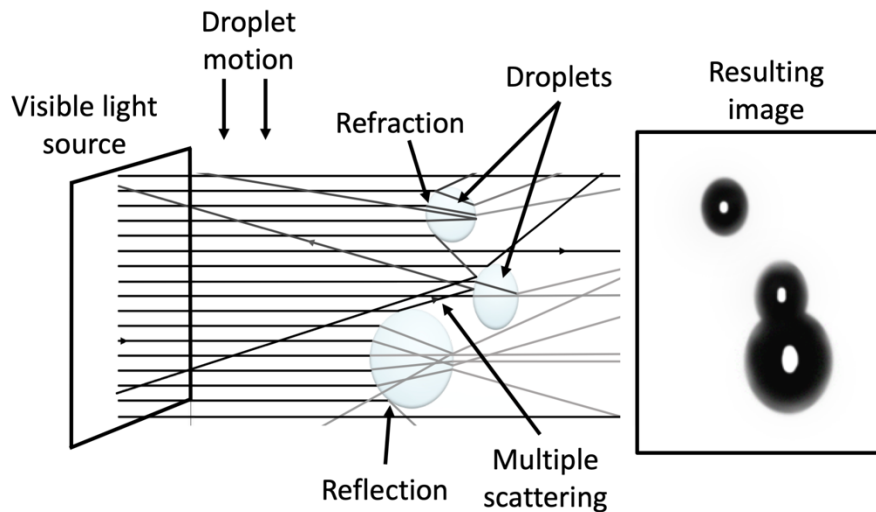
115

116 *2.2 Shadowgraphy*

117 High-speed back-illuminated imaging and shadowgraphy have been widely used for
 118 studying sprays because the interfaces between the liquid and gas regions are easily visible
 119 (Castrejón-García et al., 2011; Stevenin et al., 2012; Westlye et al., 2017). The images generally
 120 show the entire region of interest of the spray at a high temporal resolution, which enables
 121 spatiotemporal analysis of the data. However, it is not possible to capture internal details of the
 122 spray. Additionally, dense clouds of droplets obscure the light, so they cannot be distinguished
 123 from patches of liquid.

124 Shadowgraphy experiments in this study were conducted using a red light emitting diode
 125 (LED) panel, schematically shown in Fig. 2. Although the light coming from this source was not
 126 truly parallel, as it would be in shadowgraphy, it has less than 5 degrees divergence so it was
 127 considered parallel with negligible error, for simplification in the analysis. As light passes
 128 through the spray, it is reflected, refracted, and diffracted away from its original path wherever
 129 liquid is present; this creates a shadow in the resulting image. Using a visible light source makes

130 shadowgraphy subject to multiple scattering, also shown in Fig. 2, where the light reflects and
131 diffracts off of multiple droplets, decreasing the sharpness and contrast of the resulting image.
132 The high curvature of droplets also tends to act as a lens, focusing light to the center of the
133 shadow, which results in a bright spot in the center of larger droplets.
134



135
136 Figure 2: Shadowgraphy: High-speed imaging using visible light to capture a still shadow of a
137 spray (schematic not to scale).

138
139 *2.3 X-ray Imaging*

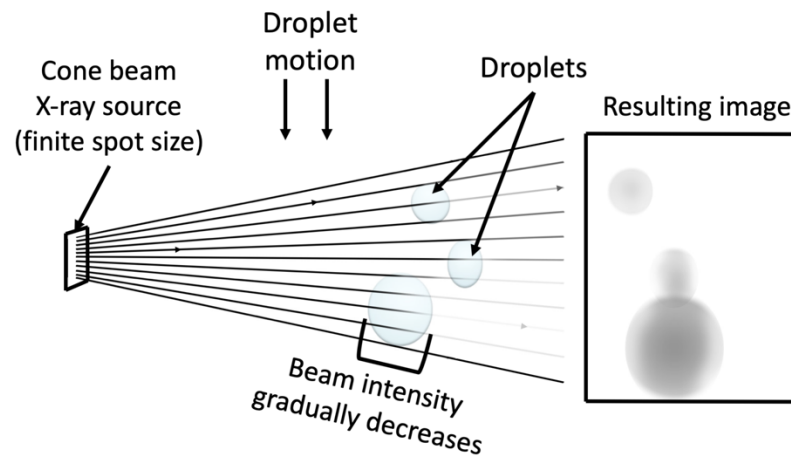
140 Another current method of imaging sprays uses X-rays rather than visible light (Heindel,
141 2018). The primary advantage of this type of measurement is that the X-rays attenuate (but not
142 reflect and barely refract) as they pass through liquid, greatly reducing refraction and multiple
143 scattering. The resulting images provide internal details of the spray. This study compares the
144 images taken from two types of X-ray producing devices, a tube source and a synchrotron. The
145 two are considered independently because of the difference in how they produce X-rays and the

146 large disparity in the radiation intensity the sources produce, which leads to different types of
147 X-ray measurements.

148 *2.3.1 Tube Source X-rays*

149 Tube source X-rays are produced when electrons are accelerated with a high voltage
150 electric field in a cathode ray tube where the electrons impact a metal target (anode) which
151 decelerates the electrons, emitting radiation in the X-ray spectrum. Figure 3 schematically shows
152 the tube source X-ray setup used in current experiments at Iowa State University's X-ray Flow
153 Visualization Laboratory, which has been described in detail elsewhere (Heindel et al., 2008).
154 The X-ray source has a cone-shaped beam and contains a wide range of photon energies, referred
155 to as broadband X-rays or white-beam X-rays. As the beam propagates through the spray, a
156 fraction of the photons are absorbed by the liquid so that the beam intensity decreases; the
157 decrease is a function of the fluid medium, the amount (path length) of fluid, and the X-ray
158 photon energy. Rather than using the equivalent path length (EPL) of the spray, calculations
159 from tube source radiography use the optical depth values directly which are equivalent to
160 $\mu \cdot \text{EPL}$, where μ is the X-ray attenuation coefficient (Li et al., 2019). Note that μ is a function of
161 the material through which the X-rays pass, as well as the wavelength of the X-ray energy, and is
162 typically tabulated for monochromatic X-ray sources, but is a complicated function for
163 polychromatic X-ray sources common in tube sources. The relatively low intensity of the tube
164 source used in this study requires an exposure time of 20 ms, and acquisition speeds of the order
165 of 10 FPS, which are too slow to capture fast-moving events, so the resulting images become
166 blurred. The blurring makes it difficult to interpret individual images, but these can be time-
167 averaged for mean spray measurements. Additionally, the tube source has a relatively large focal
168 spot, which results in a non-negligible penumbra effect (caused by X-rays hitting the same spot

169 on an occluding object from different angles), causing blurred edges. One advantage of the tube
170 source is the larger X-ray beam, which allows the entire spray region to fit inside the beam at one
171 time. The field of view for radiographs in this study was 22.5×26 mm, the tube voltage was
172 50 keV, and the current was 2.0 mA. More details about the tube source X-ray setup can be
173 found in Heindel et al. (2008) or the setup of Li et al. (2018).
174



175
176 Figure 3: Tube source radiography: The X-ray beam projects at a cone angle and the intensity
177 decreases in the presence of liquid. The resulting image can be correlated to local
178 projected mass distribution (figure not to scale).

179
180 *2.3.2 Synchrotron X-rays*

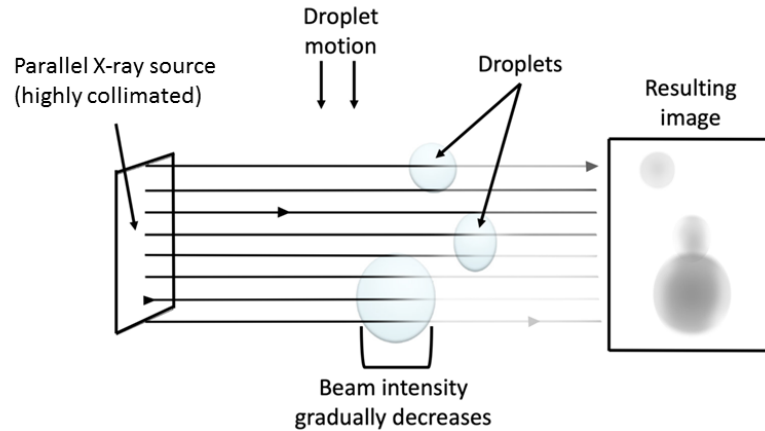
181 The synchrotron beamline used for the measurements in this study was the 7-BM
182 beamline at the Advanced Photon Source at Argonne National Lab; the setup is detailed
183 elsewhere (Kastengren et al., 2012; Heindel, 2018). The synchrotron source provides extremely
184 intense X-rays with an energy range of 5.1-12 keV that are created by fast-moving electrons
185 when they are steered by bending magnets or undulators. Using this X-ray source for

186 radiography of sprays is advantageous because the high X-ray intensity enables microsecond
187 exposures and kilohertz frame rates. This permits the acquisition of time-resolved measurements
188 or images, which allows for the capture of dynamic events and minimizes motion blur. The beam
189 is also highly collimated, which minimizes the penumbra effect, and increases the phase-contrast
190 effect.

191 *2.3.2.1 Synchrotron white-beam imaging*

192 White-beam phase-contrast imaging is named because the beam is not a single
193 wavelength but, instead, uses the broadband emission from the X-ray source. The phase-contrast
194 effect is caused by refraction and Fresnel diffraction where a relatively large propagation
195 distance increases the intensity of phase boundaries. The white-beam phase-contrast X-ray setup
196 is shown in Fig. 4. The beam is highly collimated and the source is approximately 35 m from the
197 test section. The maximum beam size is approximately 6×8 mm. As the beam propagates
198 through the spray, the intensity decreases. This concept is shown for the droplets in Fig. 4 as
199 each of the lines, representing a section of the beam, decreases in intensity depending on the path
200 length of liquid through which it passes. After going through the spray, the beam illuminates a
201 scintillator (not pictured), which creates a visible light image proportional to the incident X-ray
202 intensity. The visible light image is then reflected off a mirror and captured by a high-speed
203 camera. Additional details of white-beam phase-contrast imaging are presented by Heindel
204 (2018).

205



206

207 Figure 4: Synchrotron X-ray imaging: The nearly parallel X-ray beams pass through a spray
208 where the intensity decreases, dependent on the amount of liquid through which they
209 pass. In actual images, the edges are enhanced by a bright region around the droplets
210 (phase-contrast effect, not shown in this figure). The resulting image can be
211 correlated to the local projected mass distribution (figure not to scale).

212

213 2.3.2.2 Synchrotron focused-beam radiography

214 Focused-beam radiography in this study was performed by first filtering the white-beam
215 into a monochromatic beam, and then focusing the beam into a small cross-sectional area of
216 $5 \times 6 \mu\text{m}$ at 8 keV. The resulting beam was then raster-scanned across the spray to acquire line-
217 of-sight measurements. For focused-beam radiography, as the beam passes through the spray, it
218 reduces in intensity in the same way as white-beam imaging. After passing through the spray, the
219 X-ray beam illuminates a PIN diode that produces a voltage, proportional to the beam intensity,
220 which is then recorded. By scanning across the spray, intensity as a function of time signals are
221 recorded at multiple locations. Focused-beam radiography can be highly time-resolved. In this
222 study, focused-beam radiographs are taken at an effective frequency of 270 kHz for 10 sec. at
223 each line-of-sight location in the spray.

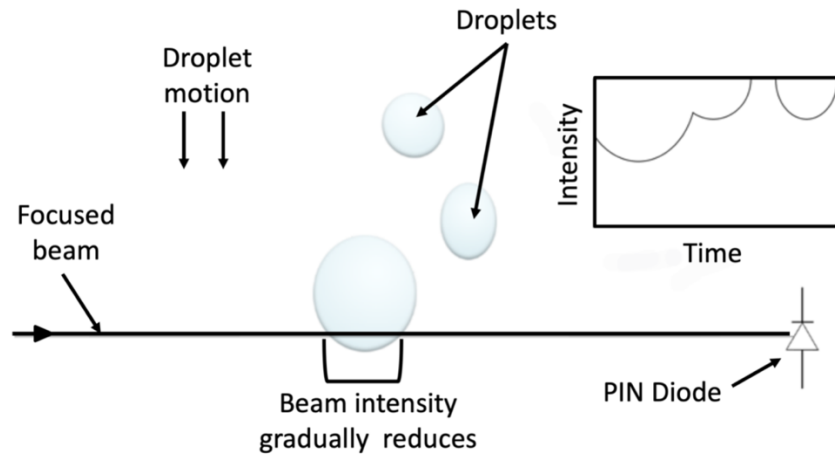
224 Because this setup requires the beam to be focused to a small cross-sectional area, the full
225 power of the beam is not required, which enables the use of a nearly monochromatic X-ray
226 beam. This greatly simplifies the subsequent analysis, since X-ray absorption is strongly
227 dependent on X-ray wavelength. A monochromatic beam eliminates beam hardening
228 (preferential absorption of lower energy radiation) so that Beer-Lambert's Law provides an
229 accurate measure of the EPL:

$$230 \qquad \qquad \qquad \text{EPL} = (1/\mu) \ln(I_0/I) \qquad \qquad \qquad (7)$$

231 where I_0 is the incident beam intensity, I is the beam intensity after passing through the spray,
232 and μ is the X-ray attenuation coefficient. By knowing the X-ray photon energy, the attenuation
233 coefficient can be obtained from the NIST XCOM database (Berger et al., 2010) which is then
234 used to obtain the equivalent path length (EPL). Being able to compute the instantaneous EPL of
235 the liquid makes it possible to measure the mass distribution of the spray, as well as for
236 additional spray dynamic properties to be computed.

237 The setup for focused-beam radiography is shown in Fig. 5. The inset of the figure shows
238 a representative measured beam intensity over time, changing as the droplets pass through the
239 probe volume. A spherical droplet yields an elliptical curve whose minimum corresponds to its
240 diameter when it is intersected at its center. Droplets that are in the same line of sight result in
241 the superposition of multiple droplets in the measurement, giving more complex results and
242 making it difficult to distinguish the signal from each droplet.

243



244

245 Figure 5: Focused-beam radiography: Intensity of an X-ray beam, that has been focused down
 246 to a small cross-sectional area, decreases following Beer-Lambert's Law as it passes
 247 through liquid (figure not to scale).

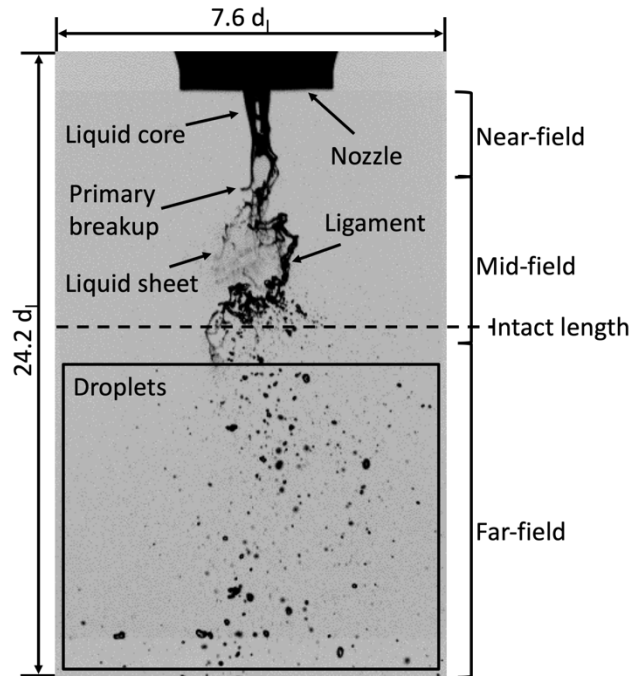
248

249 **3. Results**

250 *3.1 Shadowgraphy*

251 A shadowgraph image of the spray is shown in Fig. 6 where many of the visible spray
 252 characteristics are identifiable. The liquid core is nearest to the nozzle and characterized as a
 253 continuous section of thick liquid that has not yet broken apart. Primary breakup can be seen,
 254 leading to the formation of ligaments and liquid sheets. As ligaments move further downstream,
 255 they break up into large droplets while liquid sheets break into smaller droplets. Once the
 256 primary breakup process is finished and the liquid moves to the mid-field region, the spray has
 257 become more dilute and broken into droplets that continue to split apart as the turbulent gas flow
 258 advects them downstream. When using shadowgraphy, large particles can be seen, but their
 259 smaller neighbors often go unobserved because of the low contrast at that scale and the
 260 insufficient spatial resolution. Additionally, a percentage of smaller droplets is not captured

261 when the light source is not perfectly parallel. The minimum resolvable object size measured for
262 this setup was 0.25 mm.



263
264 Figure 6: Instantaneous shadowgraph image from a high-speed spray sequence, taken at
265 $Re_l = 1,100$ and $Re_g = 21,200$ with a frame rate of 10 kHz and exposure time of $1 \mu s$.

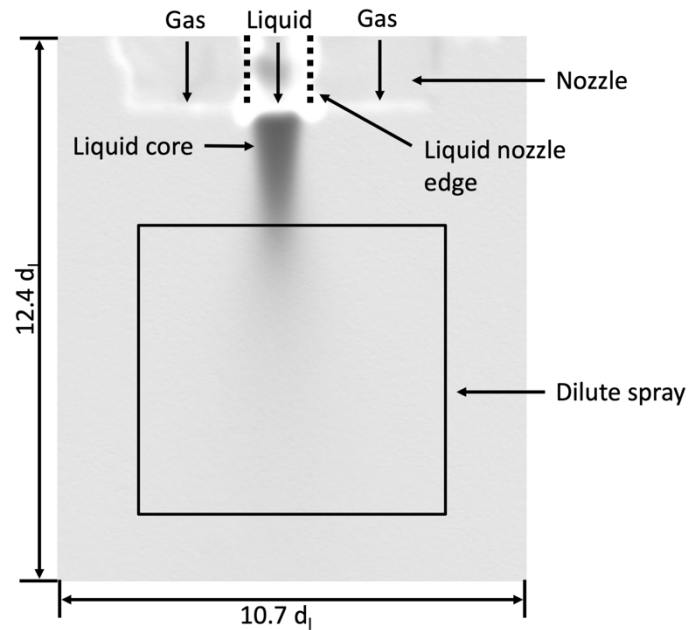
266
267 For this study, from the grayscale shadowgraph, where the background was light and the
268 liquid was dark, image thresholding was used to create a binary image that defined the gas-liquid
269 interface. However, the center region of the liquid droplets and the liquid jet core were lighter or
270 the same intensity as the background because the liquid acted as a lens and focused the
271 illumination; this was corrected through image processing when binarizing the images. A global,
272 bimodal threshold that minimized the weighted within-class variance was applied to all images,
273 which provided binary images with minimized thresholding error. After identifying the location
274 of the liquid, the intact length (longitudinal extent of the instantaneous section of liquid still fully

275 attached to the nozzle) from each image was averaged together. The error in intact length
276 measurements from shadowgraphy images was calculated to be 15% by Charalampous et al.
277 (2016) for a spray with a more dense droplet field, so the experiments here are estimated to have
278 at or below 15% measurement error. The average intact length as determined by shadowgraphy
279 for varying flow rates will be compared to other methods below.

280 *3.2 Tube Source X-rays*

281 A time-average tube source X-ray radiograph, representative of the images taken for this
282 study, is shown in Fig. 7. The canonical nozzle is the bright region along the top of the image,
283 and the image has been normalized to emphasize the spray region, which appears as the dark
284 region. The spray in the original tube source radiograph is close to a time-average image because
285 the exposure time of 20 ms long compared to flowfield time scales. The darker regions represent
286 a longer liquid pathlength, and the lighter regions represent less attenuation by the liquid. To
287 increase the contrast between the liquid and the gas background, the liquid was doped with
288 potassium iodide (KI) at a concentration of 20% by mass, which provides measurements with an
289 estimated measurement error of 5%. Past studies have shown that a KI concentration of up to
290 20% has a negligible effect on the density and viscosity of water, and a KI concentration of 20%
291 by mass does not affect beam hardening (Halls et al., 2014). The image shown in Fig. 7, at a
292 resolution of 327×377 pixels, covers an area that is $10.7 \times 12.4 d_l$ (22.5×26 mm), and is from a
293 video sequence that was acquired at a rate of 10 FPS using a Photron FastCAM Mini AX50.

294



295

296 Figure 7: Tube source X-ray radiograph. Single radiograph normalized to emphasize the spray
297 region showing the liquid mass distribution for the entire flow field region of interest.

298 The momentum flux ratio was 6.0 with an image capture rate of 10 FPS. Gas and
299 liquid conditions are $Re_l = 1,100$ and $Re_g = 21,200$.

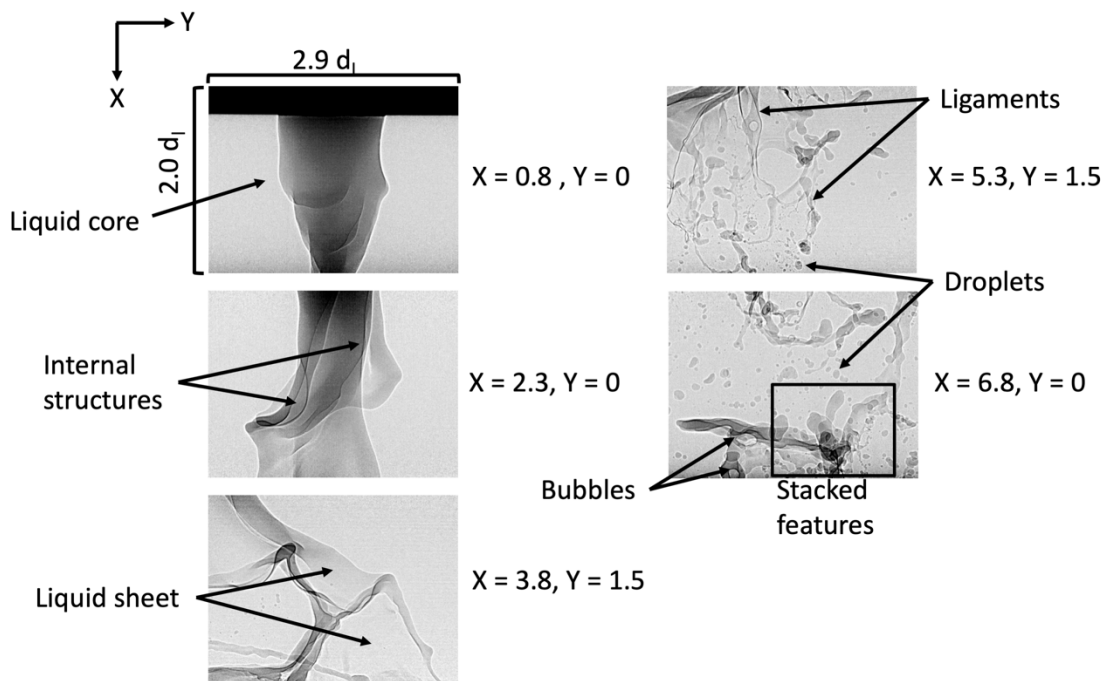
300

301 A flat-field correction was first used to reduce the fixed noise pattern and then averaged
302 over several seconds, to get a mean picture of the spray attenuation. The optical depth is used in
303 these measurements because the X-ray attenuation coefficient is not precisely known for the
304 broadband tube source (Li et al., 2019).

305 3.3 Synchrotron White-Beam Imaging

306 Figure 8 shows several synchrotron white-beam images from locations along or near the
307 centerline of the spray. Each image has an exposure time of $1.05 \mu s$ and was taken from a series
308 of X-ray images that were captured at a rate of 6 kHz with a Photron FastCAM Mini AX50. The
309 images were taken at different locations along the spray, as the beam size is much smaller than

310 the width of the spray; thus, they could not be taken synchronously. This highlights a notable
 311 difference with the tube source X-ray imaging used in this study. The tube source was able to
 312 image the spray in its entirety, but at a slower frame rate and lower flux, whereas the synchrotron
 313 white-beam imaging provided high-speed high-resolution images but over a smaller field of
 314 view. The synchrotron beam was setup for phase-contrast imaging in this study, which enhances
 315 the edges of phase differences, making the liquid-gas interface more clearly delineated.
 316 However, the analysis presented below does not use the phase-contrast effect, but rather treats
 317 the technique as attenuation only imaging.
 318



319
 320 Figure 8: Synchrotron white-beam X-ray images were taken near, or along the centerline
 321 ($Y = 0$) while the X distance increases with $X = 0$ corresponding to the jet exit. X and
 322 Y locations were non-dimensionalized by d_i , and identify the image center.
 323 $Re_l = 1,100$ and $Re_g = 21,200$ with a capture rate of 6 kHz and an exposure time of
 324 $1.05 \mu s$.

325

326 Unique spray characteristics are distinguished in each image. Unlike shadowgraphy that
327 mostly shows a binary representation of the liquid location, synchrotron X-ray imaging measures
328 the optical depth, which is related to the amount of liquid that is present in the projected image.
329 Hence, the ability to do high-speed X-ray imaging provides more details and highlights many
330 spray features that are not observed with other imaging methods, such as overlapping droplets
331 and liquid features. The liquid core in the spray shown here was more complex than a simple jet
332 with bag formation, as shown in Fig. 6 with shadowgraphy. The phase-contrast image at the
333 nozzle exit ($X = 0.8$, $Y = 0$) shows the initial formation of bags and ligaments, even before one
334 nozzle diameter away from the nozzle exit plane. Moving downstream ($X = 2.3$, $Y = 0$), internal
335 structures of the core continue to be seen as bags start to form. Then, the spray begins to form
336 thin liquid sheets and ligaments ($X = 3.8$, $Y = 1.5$) which break apart as they advect downstream
337 to form small and large droplets, respectively. One particular challenge with high-speed X-ray
338 imaging is that specific flow features are all imaged in the same projection, shown as “stacked
339 features” in Figure 8 ($X = 6.8$, $Y = 0$). However, one example of the unique features of this
340 imaging method is the ability to capture air bubbles within the liquid region ($X = 6.8$, $Y = 0$).

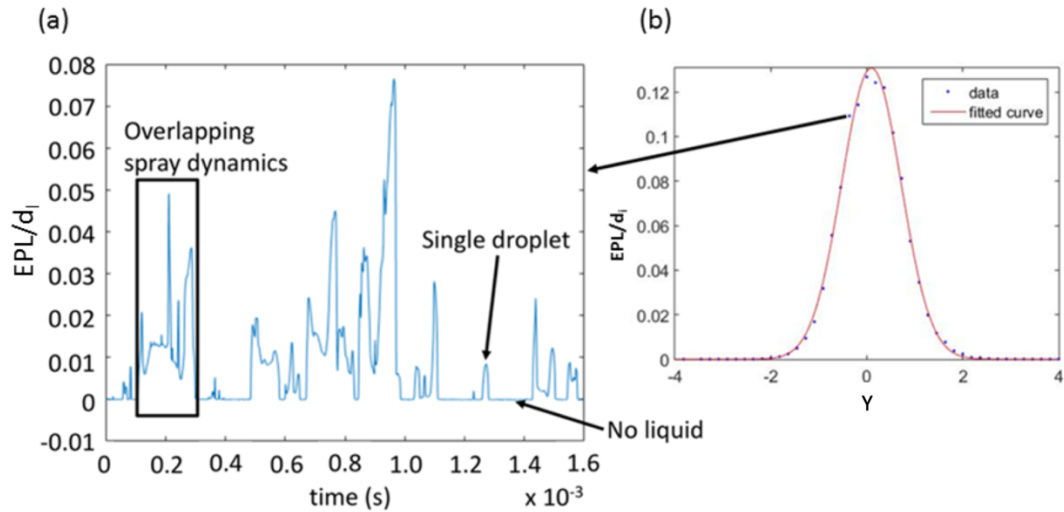
341 *3.4 Synchrotron Focused-Beam Radiography*

342 Synchrotron focused-beam radiography provides an X-ray intensity measurement as a
343 function of time. In this study, an effective signal acquisition rate of 270 kHz over a 10 sec.
344 period was recorded at each raster scan location. The instantaneous intensity signal is then used
345 with Beer-Lambert’s Law (Eq. (7)) to determine the instantaneous equivalent path length (EPL).
346 Averages at each location were used to obtain contour maps of the spray over the entire flow
347 field. Because data were taken at discrete locations, the data were linearly interpolated to

348 estimate the EPL values between acquisition locations. For the given flow conditions, the
349 maximum EPL was larger than the inner diameter of the liquid nozzle, showing that the liquid
350 spreads out slightly after leaving the nozzle, wetting the outer liquid needle surface, so the initial
351 jet diameter is approximately equal to the outer needle diameter, but still remains intact. This is
352 confirmed by images from synchrotron white-beam phase-contrast imaging (Li et al., 2017).
353 Using the same method as Kastengren et al. (2008), the absorption coefficient in Beer-Lambert's
354 law has an uncertainty of approximately 1.5%, and the measurement positions have an axial
355 uncertainty of $\pm 20 \mu\text{m}$ and a spanwise uncertainty of $\pm 5 \mu\text{m}$. The total measurement uncertainty
356 is therefore estimated to be $\pm 3.2\%$.

357 A sample of the instantaneous EPL from focused-beam data at $(X, Y) = (2.38, -0.48)$
358 from a short time span (1.6 ms) is shown in Fig. 9a. These data were acquired by raster scanning
359 across the spray and pausing at each data point location for 10 seconds to collect data, which was
360 long enough to gather good statistical data for the time-varying system. From plots like these, the
361 times when there was no liquid present are evident because the equivalent path length is very
362 near zero. Individual droplets passing through the focused-beam are easily identified by elliptical
363 curves in EPL. For much of the signal, however, the precise spray dynamics are difficult to
364 discern because the signal is composed of several overlapping projected liquid dynamics; one of
365 these regions is identified in Figure 9a as overlapping spray dynamics.

366



367

368 Figure 9: Focused-beam PIN diode signal, with $Re_l = 1,100$ and $Re_g = 21,200$: (a) a short
 369 sample of focused-beam data showing the instantaneous effective path length as a
 370 function of time, taken at $X = 2.38$ and $Y = -0.48$ and (b) the average EPL/d_i from one
 371 scan across the spray at $X = 2.38$.

372

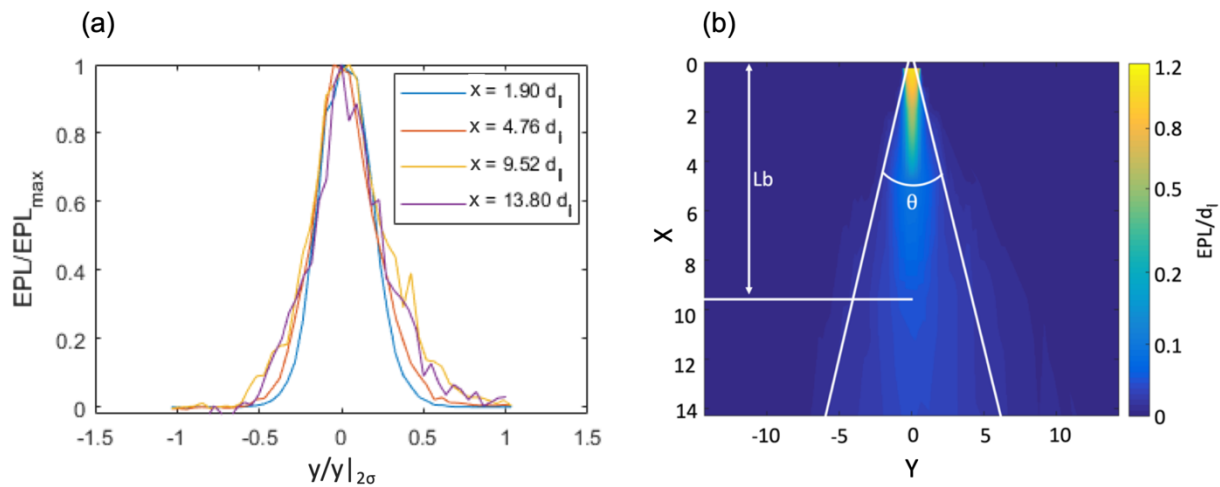
373 3.5 Self-Similarity

374 To determine if the spray angle can be accurately described as the angle between two
 375 straight lines, it was first necessary to determine if the spray was self-similar and widening in a
 376 linear fashion. It has been established that the quantity of liquid present in the cross-sectional
 377 area of a spray field can be described by a self-similar Gaussian curve in the mid-field region
 378 (Powell et al., 2000; Yue et al., 2001). The Gaussian distribution follows the velocity in single-
 379 phase jets (Van Wissen et al., 2004).

380 Using focused-beam raster scans that span the width of the spray, a Gaussian curve fit
 381 accurately represented the EPL data in the span-wise direction for all cases of the spray that were
 382 tested with data that were taken $1d_i$ or farther from the nozzle exit plane. To visualize the self-
 383 similarity of the data, the EPL was scaled so that:

384
$$EPL_{scaled} = EPL(x,y)/EPL(x)_{max} \quad (8)$$

385 where $EPL(x)_{max}$ was the maximum EPL at each axial (x) location. Additionally, the EPL
 386 distributions were scaled for the spray width using the Y location corresponding to 2σ where σ is
 387 the standard deviation, so that $y_{scaled} = y/y|_{2\sigma}$. This scaling collapsed all the data, proving self-
 388 similarity. A sample of the scaled data for $Re_l = 1,100$ and $Re_g = 21,200$ is shown in Fig. 10a.
 389



390
 391 Figure 10: $Re_g = 1,100$ and $Re_l = 21,200$, showing (a) self-similar jet profiles, scaled by EPL_{max}
 392 and 2σ , and (b) average EPL/d_l contour map showing the jet spreading angle, θ , and
 393 the intact length, L_b .

394
 395 *3.6 Spray Angle Comparison*

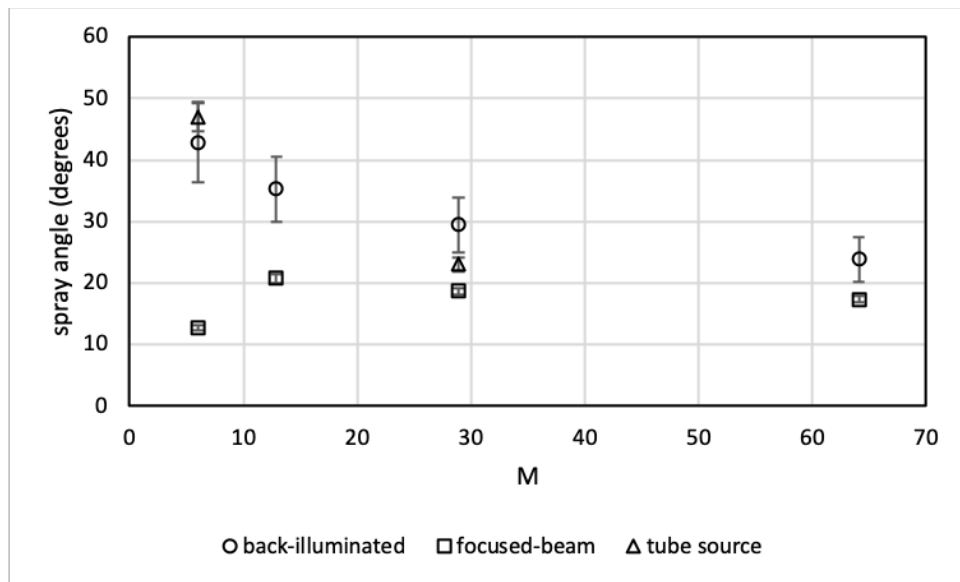
396 The results from focused-beam radiography, shadowgraphy, and tube source radiography
 397 were all used to create a time-averaged spray map. For focused-beam radiography, the average
 398 spray map represented the average EPL, as shown in Figure 10b. For shadowgraphy, the average
 399 spray map was an average of binarized images representing the probability of the presence of
 400 liquid. For tube source X-rays, the average spray map represented the averaged intensity which is

401 linked to the optical depth, and was created after individual images were normalized with the
402 background intensity, shown in Figure 7. The phase-contrast imaging presented here does not
403 provide sufficient information to calculate the spread angle because the phase-contrast imaging
404 region did not capture the entire spray. Stitching phase-contrast images together was not possible
405 because the incident X-ray flux from the synchrotron varied with time, producing non-uniform
406 background intensities from one imaging region to another. The period of the X-ray flux
407 variance ranged from milliseconds to several hours and developing a method of adjusting images
408 based on the flux variance was beyond the scope of this study.

409 At any given axial location, a Gaussian curve fit was applied to the data and the y-
410 location of 2σ from the Gaussian curve was defined as the edge of the spray for this study. The
411 spray angle was then defined as the angle between the two lines that connect the 2σ locations.
412 This angle is shown as θ for $M = 6.0$ in Figure 10b. Using the 2σ location as the spray edge is an
413 arbitrary choice, but is valid for comparison because the angle would scale with the Gaussian
414 distribution so that the spray angle for any σ location could be calculated by multiplying the
415 current spray angle by a constant.

416 Comparing the spray angle obtained from shadowgraphy, focused-beam radiography, and
417 tube-source radiography gives different results for low gas momentum flux ratios. At higher gas
418 momentum flux ratios, the results are much closer for all three methods, as shown in Figure 11.
419 At low momentum flux ratios, as the spray progresses further downstream (beyond the
420 measurements from focused-beam radiography) the spray angle increases. This explains the
421 larger spray angle for shadowgraphy and tube-source radiography, because they both captured a
422 larger spray field of view. As the gas momentum flux ratio increases, the spray angle found from
423 the three methods are more similar because the physical extent of the near-field becomes smaller

424 and the three imaging methods capture the same physics in their different fields of view. This
 425 shows that the spray edge at lower momentum flux ratios are not completely straight. Improved
 426 measurements would have focused-beam measurements further downstream, to ensure the same
 427 spray field for all measurement techniques. The most accurate value of the spray angle is found
 428 through focused-beam radiography because of the high precision of the measurements. The angle
 429 found from tube-source radiography is more accurate than shadowgraphy since the average map
 430 of shadowgraphy shows the presence or not of liquid, rather than the amount of liquid. However,
 431 the high correspondence between tube-source measurements and shadowgraphy show that the
 432 probability map found from shadowgraphy could be used with acceptable accuracy for finding
 433 the spray angle at high momentum flux ratios.

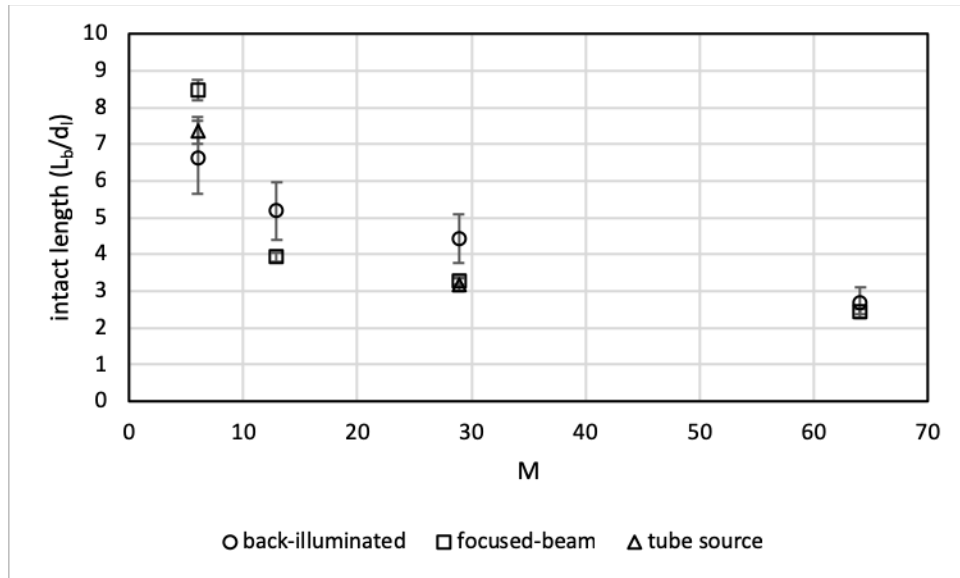


434
 435 Figure 11: Comparison of spray angle for multiple testing techniques at varying momentum flux
 436 ratios, where the error bars represent the estimated experimental error.

437

438 *3.7 Intact Length Comparison*

439 The intact length (L_b) of a spray is defined as the average axial length at which the liquid
440 remains attached to the nozzle. This attachment is either caused by a liquid core or ligaments that
441 remain connected to the liquid at the nozzle tip. The intact length for shadowgraphy ($L_{b,SI}$) was
442 computed by measuring the intact length from a series of images using image processing to
443 determine the longitudinal extend of the liquid core on each instantaneous image. The lengths
444 were then averaged, as shown in Figure 12, for varying gas momentum flux ratios. Visual
445 inspection of the intact length from the image series showed minimal error from detached
446 ligaments and droplets that obscured the measurement, even in sprays with higher momentum
447 ratios where droplet clouds are present. For sprays with a denser cloud of droplets surrounding
448 the liquid core, it will often be necessary to estimate the intact length from other measurements,
449 such as X-ray radiography. The method for estimating the intact length is below.



450

451 Figure 12: Comparison of intact length for multiple testing techniques at varying momentum
 452 flux ratios, where the error bars represent the estimated experimental error.

453

454 For measurements that use the EPL, the core length has been shown to correlate to the
 455 distance where the average EPL along the centerline is 30% of the maximum EPL (EPL_{max})
 456 along the centerline of the particular spray (Lightfoot et.al., 2015). It is important to note that the
 457 core length and intact length are not the same measure and the core length does not have a
 458 consistent definition throughout the literature. However, using the same technique as Lightfoot et
 459 al. (2015), a ratio of EPL to EPL_{max} was defined that provides a reasonable estimate of the intact
 460 length. For focused-beam radiography, the ratio found that provides the most accurate intact
 461 length is $L_{b,FB} = 0.02 * EPL(x_0)_{max}$. The $L_{b,FB}$ ratio was found by determining the EPL value along
 462 the centerline, at the intersection of the intact length (as found from shadowgraphy). Because
 463 focused-beam radiographs are point measurements, if the intact length location did not lie on a
 464 point, the values between points were estimated using a linear fit between the two nearest axial

465 locations. A comparison of the results shows that a good estimate of the intact length was found
466 from focused-beam imaging, shown in Figure 12.

467 The same method was used to estimate the intact length from tube-source X-ray images.
468 The ratio of intensity along the centerline was calculated for (I/I_0) as 20% where
469 $L_{b,TS} = 0.20 * I_{max}(x_0)/I_0$, indicating that the threshold may be a function of the X-ray power and
470 spectrum. The resulting intact lengths from this method are shown in comparison to the more
471 direct measurements from shadowgraphy in Figure 12. The high correspondence between the
472 shadowgraphy and tube-source radiography intact lengths show that the estimate from tube-
473 source radiography was a reasonable estimate.

474 Phase-contrast images were not used in estimating the intact length because the field of
475 view was too small so the spray had to be imaged in sections. Thus, the core or attached
476 ligaments did not all fit into one imaging frame. Additionally, the differences in the projected
477 intensity between spray regions where the liquid core was intact and where it was broken into a
478 multitude of large liquid droplets made the detection of intact length uncertain. The intensity
479 difference could be magnified in future experiments by doping the liquid with a sensitizer,
480 similar to the KI that was added to the water for tube source X-ray imaging.

481

482 **4. Discussion**

483 Shadowgraphy required less time for data acquisition because the system was capable of
484 capturing a large portion of the flow field in a single set-up. Unlike X-ray images, shadowgraph
485 images do not show the internal dynamics of sprays or the initial bag and ligament formation, so
486 they can only be used where a binary image showing the outline of the spray will suffice.

487 Shadowgraphy is a great option for obtaining the core length of a spray and an excellent option
488 for initial testing or proof of concept testing to qualitatively assess the spray uniformity.

489 With tube-source radiography, it was not possible to capture all the same breakup
490 dynamics as with the synchrotron beam or shadowgraphy because a longer exposure was
491 required to account for the low intensity source. However, it was possible to capture the entire
492 spray region in the same image, which was not possible with synchrotron imaging. One of the
493 largest benefits of using a tube-source X-ray setup is the ease of access when compared to the
494 synchrotron source because it is possible to install a tube-source in a university or industrial lab
495 setting.

496 Synchrotron phase-contrast imaging works well for qualitative space- and time-resolved
497 analysis of the spray features. The images showed droplet formation, bubbles, ligaments, as well
498 as bag formation and breakup. An image time series (i.e., video) can also show complex breakup
499 events with internal air bubbles (Li et al., 2017). Quantitative measurements from white-beam
500 images are possible but were challenging in this study because of the small intensity differences
501 between the regions with and without liquid, and the inability to correlate objects across imaging
502 regions.

503 Focused-beam radiography yielded accurate EPL values for the near-field region of the
504 spray. They were also highly time-resolved and were used to find the equivalent path length
505 statistics. However, the line-of-sight measurements do not allow for spatial and temporal
506 information to be acquired at the same time unless the spray is highly repeatable and the data
507 acquisition system is phase-locked (which was not the case in this study). Focused-beam
508 measurements often require another experimental technique such as shadowgraphy or
509 synchrotron white-beam measurements to probe the spray in a complementary way. The

510 mechanisms of breakup can be made evident through imaging and then quantitative statistics
511 from the focused-beam measures can better quantify spray parameters.

512

513 **5. Conclusions**

514 Using focused-beam radiography, a Gaussian distribution of the EPL was found near the
515 exit plane. The Gaussian behavior continued to exist as the spray progressed downstream with
516 $EPL(x)_{max}$ decreasing and the spray width increasing. Scaling the spray based on the $EPL(x)_{max}$,
517 and the 2σ width of the Gaussian fit as the spray edge, shows the EPL distributions collapsing
518 into a single curve, proving that they are self-similar.

519 An accurate measure of the spray angle was determined using focused-beam radiography
520 and tube-source radiography. The spray angle from shadowgraph imaging provided similar
521 results to those from focused-beam radiography and tube-source radiography at high gas
522 momentum flux ratios. However, focused-beam radiography showed a smaller spray angle at low
523 gas momentum flux ratios because the angle changes downstream and the spray region that was
524 required to get a reasonable estimate at these conditions was larger than the field of view used in
525 this study for focused-beam radiography. Although the spray angle from shadowgraphy came
526 from a binary distribution of the probability of liquid intercepting the light beam, rather than an
527 average EPL, the results show that it can provide a reasonable estimate of the spray angle.

528 The intact length was most accurately determined through shadowgraphy. For focused-
529 beam radiography, a threshold value of 2% of the EPL_{max} along the centerline of the jet resulted
530 in a strong correlation with the results from shadowgraphy. The threshold value for tube-source
531 imaging that provided the most accurate intact length is 20% of the I_{max} which also showed good
532 correlation to the intact length from shadowgraphy.

533

534 **Acknowledgments**

535 This work was sponsored by the Office of Naval Research (ONR) as part of the
536 Multidisciplinary University Research Initiatives (MURI) Program, under grant number
537 N00014-16-1-2617. The views and conclusions contained herein are those of the authors only
538 and should not be interpreted as representing those of ONR, the U.S. Navy or the
539 U.S. Government.

540 A portion of this work was performed at the 7-BM beamline of the Advanced Photon
541 Source, a U.S. Department of Energy (DOE) Office of Science User Facility operated for the
542 DOE Office of Science by Argonne National Laboratory under Contract No.
543 DE-AC02-06CH11357.

544 The tube source X-ray work was completed in the X-ray flow visualization facility at
545 Iowa State University, which was developed with support from the National Science Foundation
546 under award number CTS-021637 and Iowa State University.

547

548 **References**

549 Aggarwal, S. K. (1998). A review of spray ignition phenomena: present status and future
550 research. *Progress in Energy and Combustion Science*, 24(6), 565-600.
551 Berger, M. J., Hubbell, J. H., Seltzer, S. M., Chang, J., Coursey, J. S., Sukumar, R., Zucker, D.S.,
552 Olsen, K. (2010). *XCOM: Photon Cross Section Database* (version 1.5). [Online] Available:
553 <http://physics.nist.gov/xcom> [2019, May 1]. National Institute of Standards and Technology,
554 Gaithersburg, MD.

- 555 Castrejón-García, R., Castrejón-Pita, J. R., Martin, G. D., & Hutchings, I. M. (2011). The
556 shadowgraph imaging technique and its modern application to fluid jets and drops. *Revista*
557 *Mexicana de física*, 57(3), 266-275.
- 558 Charalampous, G., Hadjiyiannis, C., & Hardalupas, Y. (2016). Comparative measurement of the
559 breakup length of liquid jets in airblast atomisers using optical connectivity, electrical
560 connectivity and shadowgraphy. *Measurement*, 89, 288-299.
- 561 Halls, B. R., Heindel, T. J., Kastengren, A. L., & Meyer, T. R. (2014). Evaluation of X-ray
562 sources for quantitative two-and three-dimensional imaging of liquid mass distribution in
563 atomizing sprays. *International Journal of Multiphase Flow*, 59, 113-120.
- 564 Halls, B., Radke, C., Heindel, T., Lohry, W., Zhang, S., Meyer, T., & Gord, J. (2013).
565 Characterization of three-dimensional dense spray visualization techniques. In *51st AIAA*
566 *Aerospace Sciences Meeting including the New Horizons Forum and Aerospace*
567 *Exposition* (p. 477).
- 568 Heindel, T. J., Gray, J. N., & Jensen, T. C., (2008). An X-ray system for visualizing fluid flows.
569 *Flow Measurement and Instrumentation*, 19(2), 67-78.
- 570 Heindel, T. J. (2018). X-ray imaging techniques to quantify spray characteristics in the near-
571 field. *Atomization and Sprays*, 28(11), 1029-1059.
- 572 Kastengren, A., Powell, C. F., Arms, D., Dufresne, E. M., Gibson, H., & Wang, J. (2012). The
573 7BM beamline at the APS: A facility for time-resolved fluid dynamics measurements.
574 *Journal of Synchrotron Radiation*, 19(4), 654-657.
- 575 Kastengren, A. L., Powell, C. F., Riedel, T., Cheong, S. -K., Im, K. -S., Liu, X., Wang, Y. J., &
576 Wang, J. (2008). Nozzle geometry and injection duration effects on diesel sprays measured
577 by X-Ray radiography. *Journal of Fluids Engineering*, 130(4), 041301.

- 578 Lasheras, J. C., & Hopfinger, E. J. (2000). Liquid jet instability and atomization in a coaxial gas
579 stream. *Annual Review of Fluid Mechanics*, 32(1), 275-308.
- 580 Lasheras, J. C., Villermaux, E., & Hopfinger, E. J. (1998). Break-up and atomization of a round
581 water jet by a high-speed annular air jet. *Journal of Fluid Mechanics*, 357, 351-379.
- 582 Law, C. K. (1982). Recent advances in droplet vaporization and combustion. *Progress in Energy
583 and Combustion Science*, 8(3), 171-201.
- 584 Li, D., Bothell, J. K., Morgan, T. B., Heindel, T. J., Aliseda, A., Machicoane, N., & Kastengren,
585 A. L., High-speed X-ray imaging of an airblast atomizer at the nozzle exit, *7th Annual
586 Meeting of the American Physical Society Division of Fluid Dynamics*, Denver, Colorado,
587 November 19-21, 2017. DOI: <https://doi.org/10.1103/APS.DFD.2017.GFM.V0026>.
- 588 Li, D., Bothell, J. K., Morgan, T. B., Heindel, T. J., Aliseda, A., Machicoane, N., & Kastengren,
589 A. L., Quantitative analysis of an airblast atomizer near-field region using broadband and
590 narrowband X-ray sources, *ICLASS 2018, 14th Triennial International Conference on Liquid
591 Atomization and Spray Systems*, Chicago, Illinois, July 22-26, 2018, Submission-ID: 141.
- 592 Li, D., Bothell, J. K., Morgan, T. B., Machicoane, N., Aliseda, A., Kastengren, A. L., & Heindel,
593 T. J. (2019). Time-averaged spray analysis in the near-field region using broadband and
594 narrowband X-ray measurements. *Atomization and Sprays*, 29(4), 331-349.
- 595 Lightfoot, M. D., Schumaker, S. A., Danczyk, S. A., & Kastengren, A. L. (2015). *Core length
596 and spray width measurements in shear coaxial rocket injectors from X-ray radiography
597 Measurements* (No. AFRL-RQ-ED-TP-2015-115). Air Force Research Lab, Edwards AFB,
598 CA, Aerospace Systems Directorate.
- 599 Linne, M. (2013). Imaging in the optically dense regions of a spray: A review of developing
600 techniques, *Progress in Energy and Combustion Science*, 39(5), 403-440.

- 601 Linne, M. A., Paciaroni, M., Berrocal, E., & Sedarsky, D. (2009). Ballistic imaging of liquid
602 breakup processes in dense sprays. *Proceedings of the Combustion Institute*, 32 II(2), 2147–
603 2161.
- 604 Machicoane, N., Bothell, J. K., Li, D., Morgan, T. B., Heindel, T. J., Kastengren, A. L., &
605 Aliseda, A., (2019). Synchrotron radiography characterization of the liquid core dynamics in
606 a canonical two-fluid coaxial atomizer, *International Journal of Multiphase Flow*, 115, 1-8.
- 607 Powell, C. F., Yue, Y., Poola, R., & Wang, J. (2000). Time-resolved measurements of supersonic
608 fuel sprays using synchrotron X-rays. *Journal of Synchrotron Radiation*, 7(6), 356-360.
- 609 Stevenin, C., Tomas, S., Vallet, A., Amielh, M., & Anselmet, F. Shadowgraphy investigations of
610 high speed water jet atomization into still air. *ICLASS 2012, 12th Triennial International*
611 *Conference on Liquid Atomization and Spray Systems*. Heidelberg, Germany, September,
612 2012.
- 613 Westlye, F. R., Penney, K., Ivarsson, A., Pickett, L. M., Manin, J., & Skeen, S. A. (2017).
614 Diffuse back-illumination setup for high temporally resolved extinction imaging. *Applied*
615 *Optics*, 56(17), 5028-5038.
- 616 Van Wissen, R. J., Schreel, K. R., & Van Der Geld, C. W. (2005). Particle image velocimetry
617 measurements of a steam-driven confined turbulent water jet. *Journal of Fluid*
618 *Mechanics*, 530, 353-368.
- 619 Yue, Y., Powell, C. F., Poola, R., Wang, J. C., & Schaller, J. K. (2001). Quantitative
620 measurements of diesel fuel spray characteristics in the near-nozzle region using X-ray
621 absorption. *Atomization and Sprays*, 11(4), 471-490.